PNAS RESEARCH ARTICLE | NEUROSCIENCE

Metabolic trajectories in developing human neocortical neurons

Gianmarco Ferri[a,1], Francesco Finamore[a,1], Francesco Greco[a,b], Alessio Zanelli[c], Fabrizia Carli[d], Alessandro Passera[a,2,3], Elisa Degl'Innocenti[a,e,4], Francesco Olimpico[a], Riccardo Ducoli[d], Agnese Sgalippa[a,5], Gian Carlo Demontis[f], Amalia Gastaldelli[d], Francesco Cardarelli[g], Marco Onorati[c], Liam A. McDonnell[a], and Maria Teresa Dell'Anno[a,6]

Affiliations are included on p. 11.

Edited by Arnold R. Kriegstein, University of California San Francisco, San Francisco, CA; received April 23, 2025; accepted February 19, 2026 by Editorial Board Member Carla J. Shatz

The shift from glycolysis to oxidative phosphorylation is a key step in neural differentiation. Yet, the timing of metabolic rewiring in the development from progenitors to neurons remains elusive, especially in human corticogenesis. To bridge this gap, here we adopted a unique cell platform based on neocortex-derived human neuroepithelial stem cells, modeling their physiological transition into functional neurons in a 4-mo longitudinal study and until the acquisition of electrophysiological competence. Using quantitative proteomics, combined with NAD(P)H fluorescence lifetime imaging and metabolomics, we investigated the entire differentiation process and describe how metabolic pathways drive cortical neuron maturation. The prevalent metabolic adaptations were then confirmed in a human neocortical specimen. This study provides a spatiotemporal map of neocortical metabolism during development and offers a framework to investigate human neurometabolic disorders.

neocortical development | neuronal differentiation | metabolism

Significance

Metabolic adjustments during corticogenesis are pivotal but remain to be fully elucidated in the human brain. This study hinges upon the utilization of bona fide neuroepithelial stem cells originated from a developing human neocortex followed throughout a 4-mo differentiation process by combining quantitative proteomics, metabolic imaging on living cells, and targeted metabolomics. Our results show how metabolism evolves until acquisition of electrophysiological competence and highlight a bimodal behavior of glycolysis in progenitor maintenance and differentiation, as well as the activation of neuroprotective machinery prior to neuronal maturation.

The human neocortex (NCX) performs several complex cognitive functions, all requiring a substantial and uninterrupted energy supply (1, 2). Notions from rodent models (3–5) have already outlined the leading role of metabolism in shaping cell differentiation; however, they may underestimate the energetic consumption of the human brain. Recent investigations on human models of neurodevelopment contributed to clarify some aspects of metabolism's role in human corticogenesis, especially since the introduction of cortico-cerebral organoids (6, 7). However, a comprehensive view is still lacking. Developmental events underlying cortex formation are tightly regulated in time and space; therefore, a metabolic longitudinal study that follows the evolution of neurogenesis could contribute to a deeper comprehension of these elements.

Ontogenetically, corticogenesis starts from a single layer of actively proliferating neuroepithelial cells in the ventricular zone (VZ). As development proceeds, neuroepithelial cells transition into radial glia cells (8, 9) which give rise to intermediate progenitors and postmitotic neurons. Newborn neurons undertake radial migration, generating the cortical plate (CP), the primordial NCX (8, 10, 11). Neuroepithelial cells primarily rely on glycolysis (Warburg effect) (12), entrusting ATP production to pyruvate conversion into lactate, rather than oxidative phosphorylation (OXPHOS) (13). Although less efficient than OXPHOS in terms of energy production, glycolysis is faster, can be oxygen independent, and provides intermediate metabolites fundamental to amino acid, lipid, and nucleotide synthesis (14). Gradually, the transition to the neuronal lineage is accompanied by tissue vascularization, augmented mitochondrial biogenesis, and rewiring of metabolic pathways, eventually culminating in the full conversion to OXPHOS. This ensures the most efficient energy production to elicit action potentials and guarantees neuronal function (15, 16). A smooth conversion from glycolysis to OXPHOS (17) is pivotal, and it is now considered a mechanism that drives neuroepithelial cell fate, rather than a mere adaptation to normoxia of later gestational stages. In fact, a failure to implement this metabolic switch results in a blockade of the neuronal maturation process and disease (18). Moreover, in mature neurons, defects in OXPHOS often contribute to neurodevelopmental disorders and changes in glucose metabolism are a hallmark of age-dependent neurodegenerative diseases (19, 20).

From a neuroenergetic perspective (21–23), a description of human corticogenesis in terms of the metabolic enzymes involved in the process is still lacking, and besides the glycolysis/OXPHOS balance, the contribution of other biochemical cascades has only been partially covered (3, 6).

Multiple experimental models are currently available to investigate the earliest stages of neocortical development, including both two-dimensional (2D) and three-dimensional (3D) systems (24, 25).

The authors declare no competing interest.

This article is a PNAS Direct Submission. A.R.K. is a guest editor invited by the Editorial Board.

[1]G.F. and F.F. contributed equally to this work.

[2]Present address: Research Institute of Medical Pathology, Vienna BioCenter, Vienna 1030, Austria.

[3]Present address: Doctoral School of the University of Vienna and Medical University of Vienna, Vienna A-1030, Austria.

[4]Present address: NeuroPSI–Institut des Neurosciences Paris–Saclay, Saclay 91400, France.

[5]Present address: Health Science Interdisciplinary Center, Sant'Anna School of Advanced Studies, Pisa 56124, Italy.

[6]To whom correspondence may be addressed. Email: mt.dellanno@fpscience.it.

This article contains supporting information online at https://www.pnas.org/lookup/suppl/doi:10.1073/pnas.2509980123/-/DCSupplemental.

Published March 31, 2026.

Here, we employed a unique cell platform based on human NCX-derived neuroepithelial stem (NES) cells established from a 6 postconception week (PCW)-old NCX. Evidence has shown that NES cells preserve a high mitotic rate, enabling expansion without immortalization, are naturally committed to neuronal differentiation and, critically, retain the transcriptional and regional profile of their in vivo counterpart (26). In this study, human NES cells were differentiated into neocortical neurons without exogenous transcription factors and were followed for 120 d in vitro (DIV), until achieving functional maturation and action potential generation.

To preserve the physiological integrity of this system, we explored human neocortical neuron differentiation from NES cells with a combination of three complementary label-free techniques: NAD(P)H fluorescence lifetime imaging microscopy (FLIM), quantitative proteomics, and targeted quantitative metabolomics. NAD(P)H FLIM is a noninvasive technique that enables repeated imaging by measuring endogenous intracellular NAD(P)H lifetime without perturbing subcellular architecture (27) and was integrated, at specific time points, with quantitative proteomics and metabolomics for a detailed description of enzyme and metabolite abundances during neuronal differentiation.

To extend our approach to three-dimensional structures and establish a spatially resolved metabolic spatial map of cortical development, we extended our analysis to human induced pluripotent stem cell (hiPSC)-derived cerebro-cortical organoids and a fetal human NCX tissue comparing these datasets to the NES cell model. This integrated analysis corroborated the established role of OXPHOS in neuronal maturation and revealed the contribution of glycolysis and pentose phosphate pathway (PPP). In addition, we examined a subset of anabolic pathways, including nucleotide synthesis cascades, lipid biosynthesis, and glycogen biosynthesis.

Collectively, this work provides a spatiotemporal map of human corticogenesis integrated with a systematic exploration of its metabolism.

Results

Temporal Profiling of Metabolic Adaptations in Neocortical Progenitor Differentiation. To provide insight into the metabolic changes that occur in NCX neural stem/progenitor cells during their differentiation, we took advantage of human NES cells derived from the NCX of a 6 PCW-old human brain (26, 28) (Fig. 1*A*).

NES cells showed immunoreactivity for SOX1 (Fig. 1*B*), SOX2 and Nestin (Fig. 1*C*), as well as for FOXG1 and OTX2 (29) (*SI Appendix*, Fig. S1 *A–C*). Moreover, NES cells preserved an intact chromosomal profile, verified by means of karyotype analysis, even after several passages in culture (*SI Appendix*, Fig. S1*D*). A preliminary exploration every 10DIV provided evidence of a progressive and asynchronous differentiation of NES cells, as previously reported (30). Prior to DIV30, SOX2 was still expressed, cell morphology was reminiscent of progenitor cells, and accordingly, mitotic events were still appreciable (*SI Appendix*, Fig. S1*E*). The first neurons started to appear at DIV20 and increased in number by DIV30, when they exhibited a more elaborate branching and immunopositivity for the postmitotic neuronal markers BCL11B and DCX (*SI Appendix*, Fig. S1*E*).

At DIV120, NES cells yielded a neuron-enriched culture characterized by the expression of the pan-neuronal proteins TUBB3 (89.0 ± 7.0%), and MAP2 (63.8 ± 3.3%) (Fig. 1 *D* and *E*). Astrocytes (Fig. 1*F*) and oligodendrocytes (Fig. 1*G*) were also generated, albeit in very low numbers compared to the neuronal population (Fig. 1*H*). Neural progeny also expressed cortical layer-specific markers (*SI Appendix*, Fig. S1 *F–K*): layer II-IV transcription factors BRN2 and SATB2 were observed (*SI Appendix*, Fig. S1 *G*, *H*, and *K*), as well as BCL11B and TBR1, markers for layers V and VI, respectively. (*SI Appendix*, Fig. S1 *I–K*). Fast voltage-gated inward ionic currents were observed starting from DIV90 (*SI Appendix*, Fig. S2 *A* and *B*), but action potential firing was not recorded before DIV120 (*SI Appendix*, Fig. S2*C*). Based on these observations, we conceived a monthly scheme based on NAD(P)H FLIM and proteomics starting from DIV0 (NES cells) until DIV120, when the neurons were considered functionally mature (Fig. 1*A*).

Accordingly, NAD(P)H FLIM was performed on living cells every 30DIV (Fig. 1*I*). NAD(P)H lifetimes measured in each pixel of the image were represented as phasors (31), in which pixels with similar lifetimes have similar coordinates in the phasor plot. This visualization enabled the tracing of a metabolic trajectory ranging from shorter lifetimes, typical of free NAD(P)H (bottom right in the phasor plot), to longer lifetimes, characteristic of NAD(P)H bound to enzymes (left in the phasor plot). Shorter NAD(P)H lifetimes are associated with glycolysis, and longer lifetimes are indicative of OXPHOS, during which NAD(P)H is frequently bound to enzymes (27, 31, 32). The assignment of a color scale to this trajectory allowed the abundance of free and bound NAD(P)H to be visualized as a false-color image, termed a metabolic map (33) (Fig. 1*I*). The average position of each phasor during the differentiation process retraced the metabolic shift over time (Fig. 1*J*) and indicated a shift from the production of reduced NAD(P)H (free form), typical of glycolysis, to an overall consumption by oxidative enzymes (OXPHOS).

Of note, the same phasor pattern was observed when NAD(P)H FLIM was applied to cortical progenitors generated from established pluripotent cells (*SI Appendix*, Fig. S3*A*) (34). hiPSC-derived NES cells (35), immunopositive for classical neural stem cell markers (*SI Appendix*, Fig. S3 *B* and *C*), were differentiated into neocortical neurons (*SI Appendix*, Fig. S3 *D–G*). NAD(P)H FLIM analysis was performed at the pluripotent stage and systematically every 30 d until DIV120. Similar to tissue-derived NES cells, hiPSC-derived NES cells also exhibited a transition toward longer lifetimes during differentiation (*SI Appendix*, Fig. S3*H*), indicative of a metabolic switch from glycolysis to OXPHOS.

To understand how the shift in lifetimes related to changes in the cellular proteome during neurogenesis, quantitative proteomics was performed at the same time points as NAD(P)H FLIM analysis using data-independent acquisition (DIA). 3,339 proteins were identified and quantified in all time points (Dataset S1) and quality control was performed to ensure the high repeatability of the data (*SI Appendix*, Fig. S4). The expression levels of the proteins were then compared and their contribution to neurogenesis investigated. Principal-component analysis (PCA) revealed that the proteomics data recapitulated the cellular transition along the differentiation trajectory mainly in component 1 (PC1) (Fig. 1*K*), with a progressive shift that mimicked the transition toward longer FLIM lifetimes. Indeed, the first 30 d of differentiation were characterized by the largest number of differentially expressed proteins (DEPs), with respect to self-renewing NES cells (DIV0), with more than 437 proteins exhibiting significant changes in expression (Fig. 1 *K* and *L*). A selection of NAD(P)H-binding proteins with the largest changes in expression between NES cells and DIV120-neurons (*SI Appendix*, Fig. S5*a*) were assessed by western blot to independently validate the quantitative LC–MS/MS data (*SI Appendix*, Fig. S5 *B–I*).

Next, we performed a cluster analysis on the changes in protein expression levels during neurogenesis in vitro. First, the Elbow

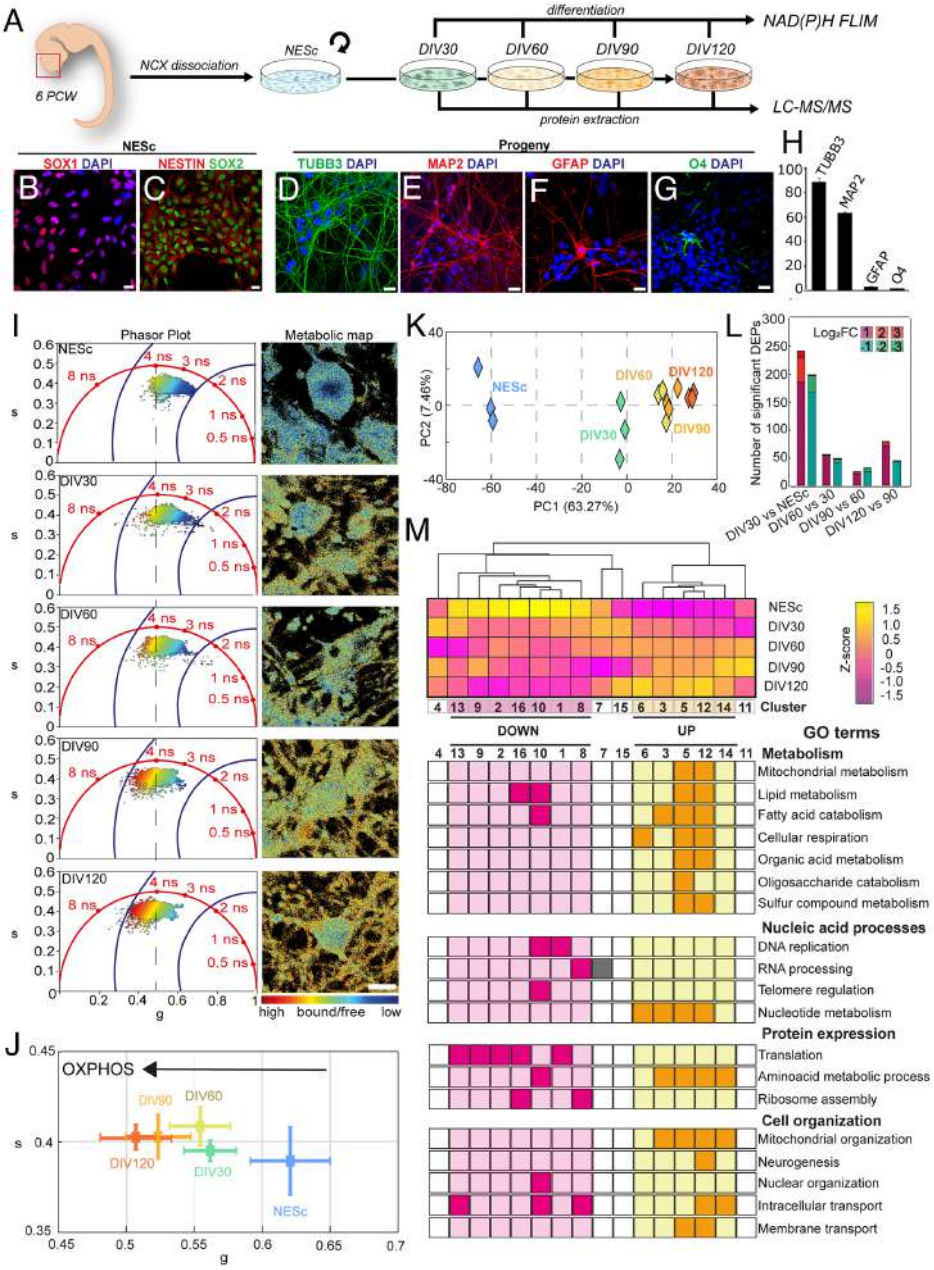

Fig. 1. Metabolic traits of human NES cell differentiation into neocortical neurons. (*A*) Schematic of the experimental protocol. NES cells (NESc) were derived from the NCX of a 6 PCW-old specimen and expanded in vitro. NES cells and their progeny underwent NAD(P)H FLIM and proteomics analysis every 30 d in vitro (DIV) until DIV120. (*B*) NES cells are immunopositive for the transcription factor SOX1 (in red). (*C*) The transcription factor SOX2 (in green) is also expressed, as well as Nestin in intermediate filaments (in red). (*D*) Neuronal progeny at DIV120 expresses pan-neuronal marker TUBB3 (in green). (*E*) Neurons exhibit MAP2+ dendritic arborization (in red). (*F*) In agreement with NES cell multipotency, GFAP+ astrocytes were observed among the neuronal progeny. (*G*) Similarly, O4+ oligodendrocytes were identified. (*H*) Quantification of the neuronal and glial markers. (*I*) Phasor plots showing the fraction of bound NAD(P)H at the different stages of neural differentiation. The metabolic maps show the cellular distribution of the NAD(P)H lifetimes. The universal circle is drawn in red. Blue arcs represent the imposed limits for the generation of the false color map as described in the *Materials and Methods* section, from dark blue (low bound/free ratio) to red (high bound/free ratio). The vertical dashed line was placed on the left edge of the phasor plot of NES cells to highlight the shift toward higher bound/free ratios during neuronal differentiation. (*J*) Scatter plot depicting the average position ± SD of the phasor coordinates g and s for each time point (n = 20 FLIM acquisitions for each time point). (*K*) Principal Component Analysis (PCA) of the proteomics data from three replicates of NES cells and their progeny at 30, 60, 90, and 120DIV. PCA shows major separation on PC1, with the greatest separation between the NES cells group and the DIV30 progeny. (*L*) Bar plot of differentially expressed proteins (DEPs, *P*-value < 0.05), colored according to fold change interval: [1,2], [2,3], >3 and [−2,−1], [−3,−2], <−3. The highest number of DEPs occurred in the early phase of neurogenesis, in the temporal frame from NES cells to the DIV30-progeny. Data are expressed as Log_2 Fold Change (FC). (*M*) Hierarchical clustering on previously clustered proteins revealed two groups with similar behavior along time points. 5 out of 16 clusters identify DEPs that are upregulated during the differentiation process (orange-yellow) and 7 out of 16 clusters are downregulated during the differentiation process (magenta). White squares indicate clusters that did not belong to the up- or downregulated groups. Gene ontology (GO) analysis represents macrocategories highlighting mitotic and translational events prevalent in NES cells, whereas biological events correlated to mitochondrial functions and cellular respiration occur preferentially in the differentiated progeny. [Scale bars: 20 μm (*B*–*G*), 10 μm (*I*).]

method (36) was applied to identify 16 clusters of protein coexpression, then followed by a fuzzy clustering algorithm (*SI Appendix*, Fig. S6). Hierarchical clustering of these temporal protein profiles was used to investigate similarities/differences. A group containing 7 of the 16 clusters exhibited decreased expression during neurogenesis. Gene ontology (GO) analysis revealed enrichment in proteins involved in DNA replication, RNA processing, and translation, consistent with the progressive loss of

self-renewal and the acquisition of a postmitotic neuronal fate. A group containing 5 of the 16 clusters exhibited increasing protein expression across DIVs, with an enrichment of the GO terms mitochondrial metabolism and reorganization, cellular respiration, and neurogenesis (Fig. 1*M* and Dataset S1). The GO term lipid metabolism included both biosynthetic and catabolic processes, with the former being prevalent in progenitors and the latter more abundant in the neuronal progeny (Dataset S1).

Of note, the transition from NES cells to DIV30 was characterized by a decisive reprogramming of cell fate. This involved a coordinated downregulation of cell cycle machinery (MCM complex, PCNA, CDK1/6) and Nestin expression concurrently with the upregulation of the epigenetic regulator MeCP2, involved in neuronal maturation (37). Moreover, several structural proteins (TPPP3, MAP2, NCAM1) (38) and synaptic components (CAPS, SYNJ1, and AMPH) (38) (*SI Appendix*, Fig. S7*A* and Dataset S1) appeared upregulated already at this stage. At DIV60, several lysosomal hydrolases (e.g., GALC, GAA, NEU1, AGA) (39) increased, suggesting a major investment in cellular maintenance and recycling, consistent with a postmitotic fate (*SI Appendix*, Fig. S7*B* and Dataset S1). Later time points (DIV90 and DIV120) were characterized by the upregulation of proteins implicated in calcium signaling (CAMK1, CALB1, CAMK2G) (40), together with proteins for synaptic function and retrograde transport (VAMP3, GAP43, and ACTR1A) (41). These late-stage changes, coupled with the action potential firing observed at DIV120, indicated a final refinement to establish a fully functional, mature neuron (*SI Appendix*, Fig. S7 *C* and *D* and Dataset S1).

Collectively, our data indicate that in the transition from NES cells to mature neurons, there is progressive increase in NAD(P)H oxidative metabolism followed by adaptations in the proteome.

Proteomic Remodeling of Respiratory Enzymes in Differentiating Cortical Neurons. Subsequently, we leveraged our proteomic dataset to conduct a systematic analysis of multiple biochemical cascades at single-enzyme resolution, starting with glycolysis as the primary glucose utilization pathway (Fig. 2 and Dataset S2).

We found that during the differentiation process, glycolytic enzymes expressed different temporal profiles (*SI Appendix*, Fig. S8 *A* and *B*). A subset of enzymes operating in the first reactions, the so-called preparatory phase, exhibited a progressive increase in abundance. Hexokinase 1 (HK1), which phosphorylates glucose (Fig. 2), increased significantly already at DIV30 (*P*-value: 0.016) and kept incrementing over time (Dataset S2). Glucose-6-phosphate isomerase (GPI), phosphofructokinase M (PFKM), and aldolase C (ALDO C), the latter known as a neuron-specific isoform (42), exhibited similar profiles (*SI Appendix*, Fig. S8 *A* and *B*).

Conversely, other glycolytic enzymes in the subsequent pay-off phase showed an opposite trend and collectively diminished their abundance in the earliest phases of differentiation (DIV30-DIV60) (*SI Appendix*, Fig. S8*B*). Exceptions were the neuronal specific isoforms enolase 2 (ENO2) (43), which expectedly was upregulated in neurons (Fig. 2 and *SI Appendix*, Fig. S8 *A* and *B*), and PKM1 (13) (*SI Appendix*, Fig. S9*A*), more expressed in neurons compared to isoform PKM2.

A notable reduction was observed in lactate dehydrogenase isoform A (LDHA), a pivotal enzyme mediating the Warburg effect in neural progenitors (13). LDHA exhibited a pronounced and statistically significant decline (*P*-value: 0.015) at DIV30, with continued attenuation over time, thereby corroborating the diminished reliance on aerobic glycolysis for neuronal energy metabolism (Fig. 2, *SI Appendix*, Fig. S8*B*, and Dataset S2).

The pyruvate produced by glycolysis enters the mitochondria by means of the mitochondrial pyruvate carrier (MPC2) and becomes a substrate for the TCA cycle. Accordingly, the relative abundance of TCA cycle enzymes progressively increased. Specifically, the enzymes aconitase 2 (ACO2), isocitrate dehydrogenase 2 (IDH2), fumarate hydratase (FH), pyruvate dehydrogenase (PDH), succinate dehydrogenase (SDH), and succinyl-CoA ligase (SUCL) exhibited a significant change (Fig. 2 and *SI Appendix*, Fig. S8*C*).

The ETC, which converts the reducing power of NADH and $FADH_2$ into ATP, becomes increasingly active in neurons (3). Accordingly, the respiratory chain complexes exhibited a significant upregulation: On average, complex I (CI) subunits started a significant augmentation at DIV30, followed by complex II (CII/SDH) subunits at DIV60 and complex IV at DIV120 (Dataset S2). Concomitantly, ATP synthase also reached its highest expression at DIV120 when neurons achieved functional maturation and action potential firing (Fig. 2 and *SI Appendix*, Figs. S2 and S8*D*).

Overall, in agreement with observations from NAD(P)H FLIM analysis, our data show that enzymes in oxidative metabolism gradually become more present in the neuronal progeny, concurrently with a bimodal rearrangement of glycolytic enzymes.

Glycolysis Bimodal Behavior Reflects Functional Partitioning between Anabolic Support and Neuronal Maturation. Beyond cellular respiration, we also explored a series of anabolic pathways. Developing progenitors heavily rely on endogenous lipid and nucleotide biosynthesis as this process is critical for their normal function and survival (44). Conversely, differentiated neurons rely on fatty acids and cholesterol being provided by neighboring astrocytes (45, 46). Accordingly, the majority of fatty acid and cholesterol biosynthetic enzymes exhibited a substantial drop in abundance during the passage from NES cells to DIV30 and kept reducing their abundance thereafter (Fig. 2, *SI Appendix*, Fig. S8 *E* and *F*, and Dataset S2).

1C metabolism provides elements for nucleic acid, amino acid, and polyamine synthesis, and produces methyl groups for DNA and histone methylation (47). Enzymes involved in 1C metabolism were found to be downregulated at the initial step of differentiation (DIV30), concomitantly with NES cells exiting the cell cycle and the initiation of the differentiation process (Fig. 2 and *SI Appendix*, Fig. S8*G*).

An alternative route to glucose oxidation is the PPP (Fig. 2), whose enzymes showed an oscillatory behavior without presenting a clear trend over the entire differentiation period, suggesting a contribution to both progenitor and neuronal progeny metabolism (Fig. 2 and *SI Appendix*, Fig. S8*H*).

In our data, enzymes in glycogen metabolism exhibited a dichotomous behavior. Key enzymes involved in glycogen preparation showed increased abundance (Fig. 2 and *SI Appendix*, Fig. S8*I*), consistent with the upregulation of HK1 and PGM1, which generate the substrate glucose-1-phosphate. In stark contrast, glycogen synthases 1 and 2 (GYS1, GYS2) were progressively depleted, in agreement with the established role of astrocytes as the primary glycogen-synthesizing cells (34, 35). Notably, differentiated neurons maintained robust expression of glycogen degradation enzymes, including α-1,6-glucosidase (AGL) and glycogen phosphorylase B (PYGB) (Fig. 2 and *SI Appendix*, Fig. S8*I*), suggesting that mature neurons preserve the machinery to utilize glycogen from neighboring glial cells when needed.

1C metabolism, PPP, and glycogen synthesis cascades are all dependent on intermediates produced during glycolysis (Fig. 2). Therefore, in order to understand whether the bimodal behavior of the glycolysis preparatory and payoff phases was mirrored in the temporal schemes of neuronal differentiation and anabolic pathways, we conducted a Pearson correlation analysis (*SI Appendix*, Fig. S9*B* and Dataset S2).

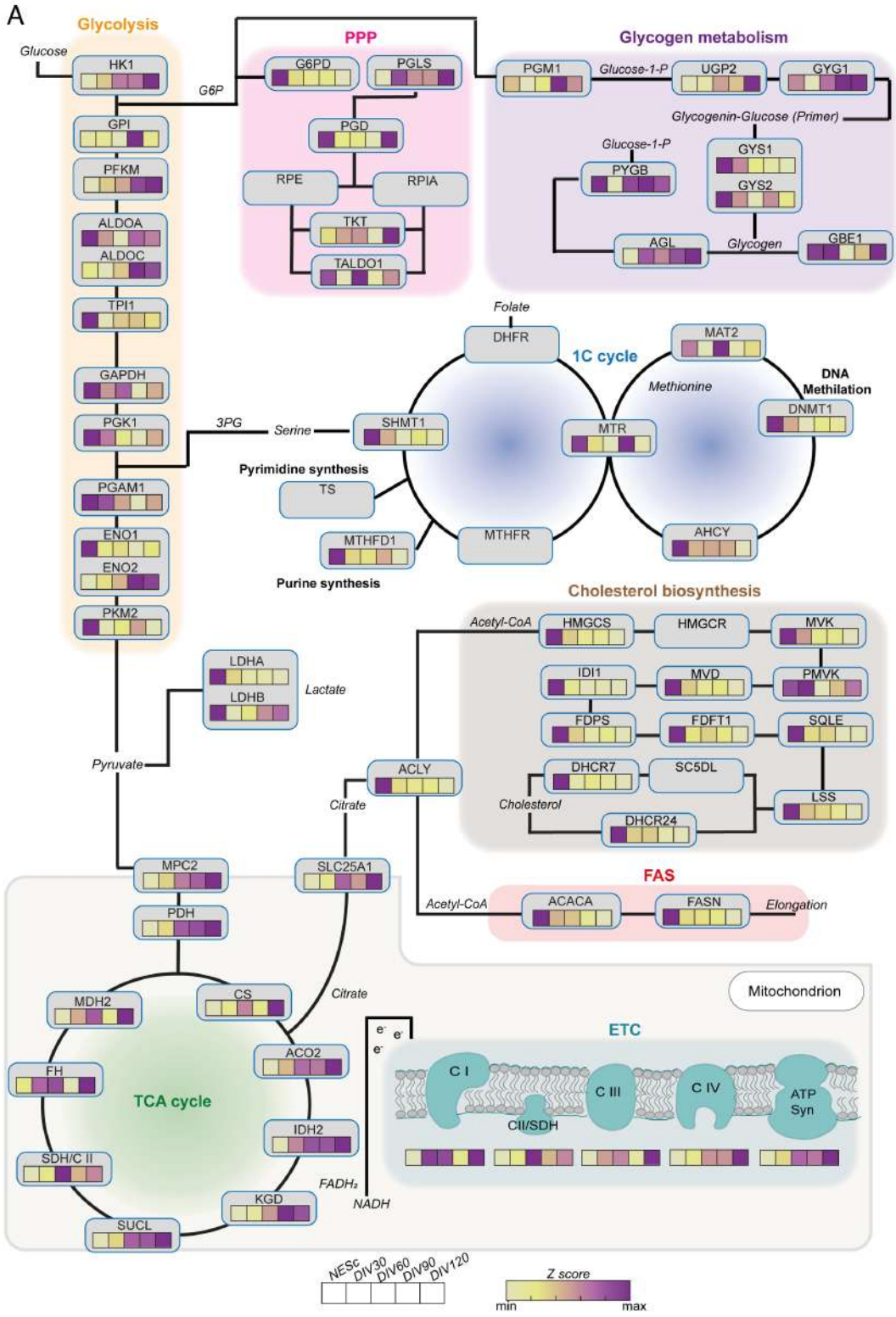

Fig. 2. Single-enzyme analysis of abundance changes of the principal metabolic pathways. (*A*) Scheme of cellular respiration process (glycolysis, tricarboxylic acid -TCA- cycle, mitochondrial electron transport chain -ETC), pentose phosphate pathway (PPP), fatty acid synthesis (FAS), Cholesterol biosynthesis, glycogen metabolism, 1 carbon (1C) metabolism and their connections. Changes in the z-score normalized abundance of key enzymes are represented with a color scale (from light to dark), if present in the proteomics dataset. The normalized abundances of each subunit of NADH dehydrogenase complex (CI), succinate dehydrogenase complex (CII) also represented in TCA cycle as SDH, cytochrome bc1 complex (CIII), cytochrome c oxidase complex (CIV), and ATP-synthase (ATP Syn.) were averaged for each time point.

Generally, enzymes catalyzing the initial steps of glycolysis, that we found being increased over time (HK1, PFKM, ALDOC), exhibited a strong positive correlation with neuronal markers (i.e., TPPP3, MAP2, NCAM1, SYNJ1, MECP2) and negative correlation with proliferative markers (i.e., MCM complex, CDK11A, CDK) (*SI Appendix*, Fig. S9*B*). Of note, this pattern was totally reversed for payoff phase enzymes (*SI Appendix*, Fig. S9*B* and Dataset S2), thereby indicating a sharp separation

in the glycolytic pathway supporting either the proliferative nature of NES cells or the differentiation of the neuronal progeny. A similar scheme emerged in the correlation analysis comparing glycolytic enzymes with anabolic cascades (FAS, PPP, 1C metabolism, glycogen synthesis, and cholesterol biosynthesis), reinforcing the segregation of glycolysis steps and the major contribution of the pay-off phases in biosynthetic events occurring in progenitors (*SI Appendix*, Fig. S9*C*).

Notably, from the correlation analysis, we observed that LDHA expression was temporally synchronized and displayed the strongest correlations (both positive and negative) with several markers. Specifically, LDHA showed robust positive correlation (0.97) with the MCM protein complex and enzymes in anabolic processes alongside strong negative correlation (−0.95) with neuronal markers involved in cytoskeletal and synaptic remodeling (*SI Appendix*, Fig. S9 *D* and *E*).

Overall, from a projection of the average temporal profiles, we inferred that glycolysis remained overall stable, after an initial inflection at DIV30, indicating a contribution also in the neuronal progeny. Simultaneously, TCA and ETC enzymes displayed a gradual increase (*SI Appendix*, Fig. S9*F*). Anabolic pathways collectively dropped, with a sharp reduction within the first 30 d (*SI Appendix*, Fig. S9*G*), indicating a rapid redirection of the energy flux. The bimodal progression observed in the glycolytic pathway was reflected in anabolic pathways and in the expression of neuronal markers, highlighting a major correlation of the payoff glycolytic phase in biosynthetic cascades.

Early Metabolic Rewiring Facilitates Sustained Antioxidant Defense in Mature Neurons. The single-enzyme analysis of the major metabolic pathways suggested a finely orchestrated remodeling process persisting across all time points. However, we observed that out of 44 metabolic enzymes exhibiting a significant change in abundance, 24 changed within the first month of differentiation (Fig. 3*A* and Dataset S3). Moreover, NAD(P)H FLIM analysis (Fig. 1 *J* and *L*) showed a major shift in the fraction of enzyme-bound NAD(P)H in the same time window (Fig. 3*B*). In this context, 69 out of the 131 NAD(P)H-binding proteins identified in our dataset demonstrated significantly altered expression at DIV30 (Fig. 3*C*). This finding suggests not only an increase in the flux of bound NAD(P)H but also a shift in the composition of proteins capable of binding it (*SI Appendix*, Fig. S10).

Collectively, these data indicated that the first month represents a critical phase in the differentiation of NES cells. We further characterized the metabolic landscape within this time window by performing gas chromatography-based metabolomics on proliferating NES cells and DIV30 progeny. To provide a comprehensive context, we quantified the concentrations of glucose and glutamine in the respective media. Glucose levels remained substantially unchanged (4.47 mg/mL at DIV0 *vs* 4.37 mg/mL at DIV30), whereas glutamine concentration was approximately twofold higher in the DIV30 medium compared to the DIV0 medium (2.05 µmol/mL vs. 1.03 µmol/mL). These variations in media formulation were carefully considered when interpreting the metabolomics differences between the two stages.

The concentrations of glucose-6-phosphate (G6P) and fructose-6-phosphate (F6P), the first two intermediates of glycolysis, increased by 26% and 50%, respectively (Fig. 3*D* and Dataset S3), thus corroborating the upregulation of the first glycolytic enzymes observed from the proteomics data (Fig. 2). The accumulation of G6P and F6P appeared to deliberately shunt carbon flux into the PPP, as also suggested by the increase in its key intermediates, including xylulose-5-phosphate (Xu5P), ribose-5-phosphate (R5P), and sedoheptulose-7-phosphate (S7P) (Fig. 3*D* and Dataset S3). PPP product NADPH allows for glutathione recycling and antioxidant defense, needed in neuronal progeny for protection against reactive oxygen species (48). In support of this, the functional interaction network of differentially expressed NAD(P)H binding proteins at DIV30 showed a GO enrichment in cellular respiration, amino acid biosynthesis, and aldehyde detoxification activity. In particular, we observed that 6 of the 19 human aldehyde dehydrogenase isoforms (49), known to be part of the neuroprotective molecular machinery (50), were increased up to threefold already at DIV30 (Fig. 3*E*).

Following the fate of oxidized glucose through glycolysis, intermediates in the subsequent steps were found to be reduced, in agreement with the lower expression of their processing enzymes (Fig. 3*F*). The quantitative metabolomics data also showed a reduction in lactate production, consistent with the concomitant shutdown of LDHA (Fig. 2; FC −1.70). In particular, the lactate/pyruvate ratio decreased by 38% (Fig. 3*G* and Dataset S3), suggesting a reduction of the Warburg effect already at DIV30. Overall, the trends observed for glycolysis intermediates aligned with the fold changes of their respective enzymes detected in the proteomic dataset in the time interval DIV0-DIV30 (Fig. 3*H*).

The concentration of TCA cycle intermediates showed a downward trend after a month of differentiation (Fig. 3*G* and Dataset S3). This metabolic profile stands in contrast with the proteomic data (Dataset S2), which showed a progressive increase in the abundance of TCA cycle enzymes over the same period.

For what concerns lipid biosynthesis, metabolomics analysis on the two fundamental building blocks of cell membranes revealed an increase in cholesterol abundance (about 85%) and an unchanged concentration of palmitate at DIV30 (Fig. 3*H* and Dataset S3). As previously shown (Fig. 2), cholesterol synthesis machinery and FAS underwent a sharp decrease in expression at this time point, in apparent contradiction with the measured concentrations of their metabolites. This aspect could be addressed by the different metabolic flux between a proliferative and a postmitotic cell. NES cells rely on high biosynthetic activity to generate the biomass required for rapid cell division. However, this high synthetic influx is continuously counterbalanced by a massive efflux due to the proliferative dilution of the entire cellular mass, including its metabolite pools. Conversely, DIV30 neurons, as postmitotic cells, lack this dilution efflux. Although their synthesis rate is lower, these building blocks are no longer partitioned for division. Instead, they are entirely dedicated to cumulative structural accretion, fueling the biogenesis of axons and dendrites over the first month of differentiation.

From the postmitotic transition to functional maturation, neuronal markers of cytoskeletal remodeling, axonal transport, synaptic function, and calcium signaling evolved alongside the metabolic shift to OXPHOS. Pearson correlation analysis between metabolic enzymes and maturation markers for DIV30 to DIV120 (Dataset S3) revealed that the downregulation of biosynthetic pathways (cholesterol biosynthesis and FAs) strongly anticorrelates with neuronal maturation (*SI Appendix*, Fig. S11*A*). Conversely, functional maturity is supported by oxidative metabolism, as evidenced by high positive correlations between neuronal markers and enzymes of the ETC, TCA cycle, and glycolysis (*SI Appendix*, Fig. S11*A*).

Key regulators of cytoskeletal stability (TPPP/3) and vesicle priming (CAPS) exhibited tight synchronization with these metabolic shifts (*SI Appendix*, Fig. S11*B*). Specifically, the temporal profiles of cellular respiration pathways and glycogen metabolism aligned with markers of dendritic development and synaptic trafficking (*SI Appendix*, Fig. S11*C*), supporting the claim that higher

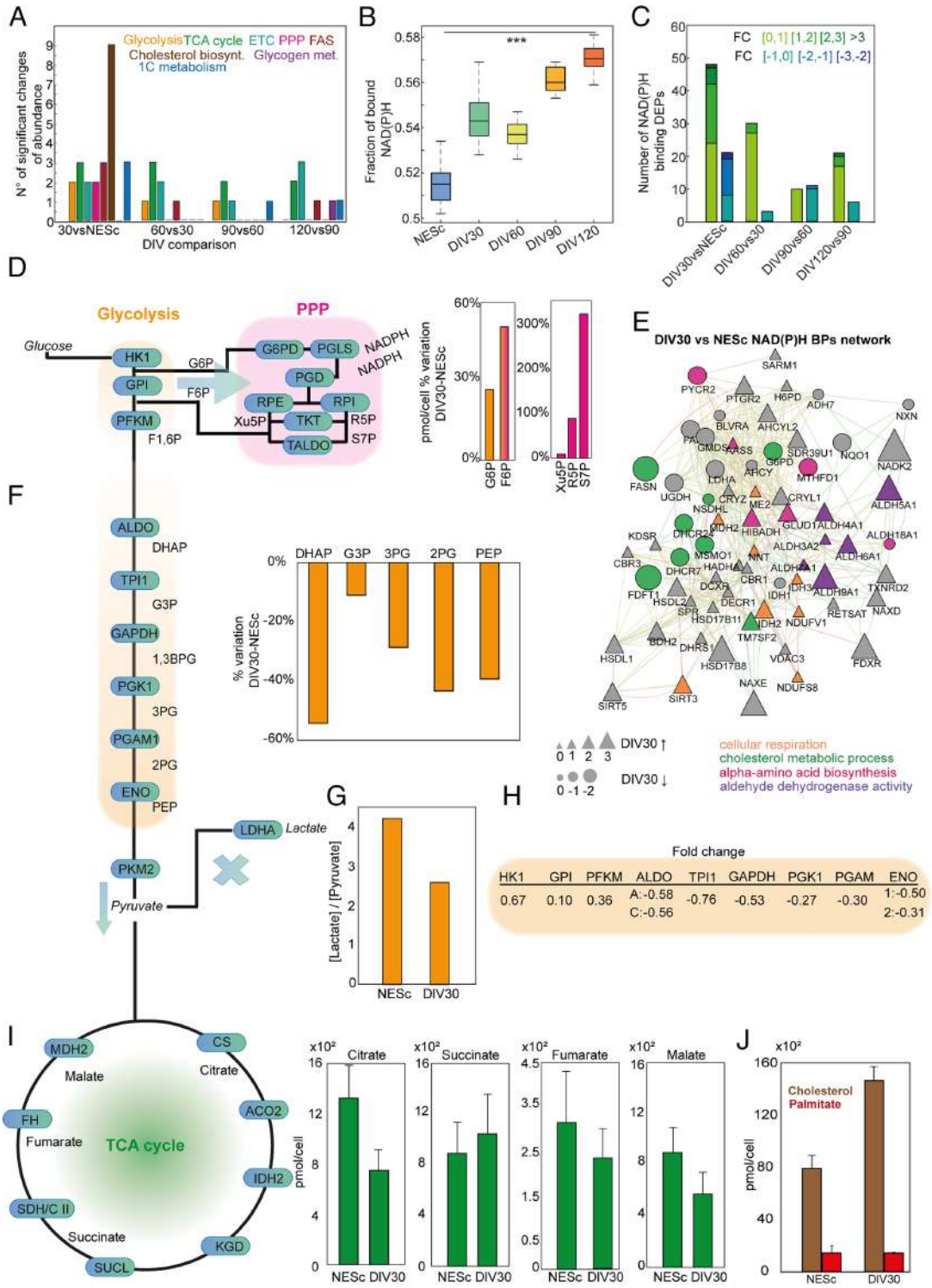

Fig. 3. Major metabolic reprogramming occurs early during NCX progenitor differentiation. (*A*) Bar plot showing the number of proteins with significant changes of abundance, separated by metabolic pathway and differentiation interval. (*B*) Box plot representing the fraction of bound NAD(P)H as revealed by NAD(P)H FLIM analysis. The bound fraction is defined as the mean geometrical distance between the experimental points of the phasor and the value on the universal circle representing free NAD(P)H with a 0.4 ns lifetime. Statistical significance was tested using a multiple comparison ANOVA test (Bonferroni corrected; ****P-value < 0.0001). (*C*) Bar plot of differentially expressed NAD(P)H-binding proteins at each differentiation interval revealing that the largest change occurred in the first 30 d (FC, fold change). (*D*) On the *Left*, scheme of the upper part of glycolysis, PPP and related metabolites. On the *Right*, percentage change in metabolite concentrations between DIV30 and NESc. G6P, glucose-6-phosphate; F6P, fructose-6-phosphate; Xu5P, xylulose-5-phosphate; R5P, ribose-5-phosphate; S7P sedoheptulose-7-phosphate. (*E*) Functional networking of differentially expressed NAD(P)H-binding proteins (BPs) in NES cells and the DIV30 progeny. Triangles indicate upregulated proteins; circles indicate down-regulated proteins. Proteins related to cellular respiration (orange) are upregulated, as well as aldehyde dehydrogenases (purple) and amino acid biosynthesis (pink). Cholesterol metabolic processes (green) are reduced. Data are expressed as Log_2 of FC. (*F*) On the *Left*, scheme of the lower part of glycolysis. On the *Right*, percentage change in metabolite concentrations between DIV30 and NESc. DHAP, Dihydroxyacetone phosphate; G3P, glyceraldehyde-3-phosphate; 3PG, 3-phosphoglycerate; 2PG, 2-phosphoglycerate; PEP, phosphoenolpyruvate. (*G*) Ratio of lactate and pyruvate concentrations in NESc and DIV30. (*H*) Abundance expressed as fold change of glycolysis enzymes in DIV30 progeny vs. NESc. (*I*) On the *Left*, scheme of TCA cycle enzymes and metabolites. On the *Right*, normalized average concentrations (n = 3 independent measurements) ± SD expressed as pmol/cell of the principal metabolites in NESc and DIV30 progeny. (*J*) Normalized average concentrations (n = 3 independent measurements) ± SD expressed as pmol/cell of cholesterol and palmitate in NESc and DIV30.

energy demands and glycogen bioavailability are essential for functional maturation. Moreover, the PPP appeared synchronized with maturation markers, corroborating the strategic redirection of NADPH production already observed in the transition DIV0 to DIV30. As NADPH-dependent cholesterol and FA biosynthetic enzyme expression declined from DIV30 to DIV120, NADPH was increasingly funneled toward reductases (GSR and TXNRD1/2), which conversely increase, to neutralize ROS generated by sustained OXPHOS activity (*SI Appendix*, Fig. S11*D*).

Collectively, these integrated analyses demonstrate that early metabolic rearrangements secure postmitotic fate and neuroprotection. In later stages, the dominance of OXPHOS over biosynthesis creates the optimal energetic and redox environment for terminal structural and functional maturation.

Temporal Evolution of NES Cell Metabolism Mirrors Spatial Features of Developing Human Neocortex. The longitudinal study on NES cells and their progeny provided an insight into the temporal variation of metabolic pathways during the differentiation of neocortical progenitors. Then, we decided to translate our analysis to a spatial dimension.

First, we took advantage of cerebro-cortical organoids to recapitulate the initial stages of neural tube development (Fig. 4*A* and Dataset S4). Neural rosettes populated by SOX2 expressing progenitors appeared framed by their RBFOX3-immunopositive neuronal progeny (*SI Appendix*, Fig. S12*A*). Similarly, the metabolic map provided by NAD(P)H FLIM revealed that the rosettes were distinguishable by a glycolytic metabolism, whereas mature neurons were identified by prevalent OXPHOS (Fig. 4*B*). This finding confirmed that the metabolic fingerprint of neural progenitors and derived neurons was effectively preserved and spatially segregated in the 3D model.

Subsequently, to provide a physiological reference for the spatial component of metabolic rearrangements operating in the developing NCX, we investigated a human neocortical tissue sample at 11 PCW using the same analytical pipeline. The mid-neurogenesis neocortical sample offered the unique opportunity to investigate concurrently progenitors and their neuronal progeny within their native tissue architecture, devoid of any culture-related artifacts. Cortical progenitors (neuroepithelial cells and radial glia cells) are located in the FOXG1-positive VZ (28) from which they migrate and differentiate into intermediate neurons, moving through the subventricular zone (SVZ) and the intermediate zone (IZ), until they reach the CP according to a well-established inside-out lamination pattern (Fig. 4*C*) (51). The metabolic map generated by NAD(P)H FLIM revealed a predominance of short NAD(P)H lifetimes in the VZ and SVZ, indicating a metabolism primarily geared to glycolysis. Gradually, from the IZ to the CP, the proportion of enzyme-bound NAD(P)H increased, indicating a shift toward oxidative metabolism in correspondence with the increasing density of postmitotic neurons, and in agreement with findings collected from the 2D model (Fig. 4*D* and *SI Appendix*, Fig. S12*B*).

To explore, at single enzyme resolution, the variation of biochemical cascades in progenitors and neurons of the human NCX, quantitative proteomics analysis was performed on cell populations from the VZ (identified by SOX2+ areas) and the CP (identified by BCL11B+ areas) (Fig. 4*E* and *SI Appendix*, Fig. S12*C*) isolated by laser-capture microdissection (*SI Appendix*, Fig. S12*D*). This led to the identification of 973 and 932 proteins that exhibited significantly increased expression in the VZ and CP, respectively (Dataset S4). GO enrichment analysis of significantly upregulated proteins in the VZ revealed terms related to DNA replication, mitosis, and biosynthetic processes (Fig. 4*F*). Conversely, the CP was mostly enriched in proteins related to neurodevelopment and cellular respiration (Fig. 4*G*).

Pathway-level enzyme expression analysis performed by Gene set Enrichment Analysis (GSEA) showed that, globally, the metabolic specialization of the two regions mirrored the trends observed in the NES cell model (*SI Appendix*, Fig. S13). Several glycolytic enzymes, such as ENO2, which exhibited the highest fold change, HK1, PFKM, and GPI were upregulated in CP cells. Conversely, PKM2, ENO1, GAPDH, and PGAM1 exhibited higher expressions in the VZ. Unlike previous observations (13, 52), and also differently from our NES cell model, the LDH isoforms exhibited small increases in expression in the CP (Fig. 4*H*). Overall, the majority of the TCA cycle enzymes and ETC complex subunits were upregulated in the CP (Fig. 4 *I* and *J*), confirming the expected shift toward OXPHOS in differentiating neurons. 1C metabolism enzymes were expectedly upregulated in the VZ (Fig. 4*K*), and enzymes for the glycogen metabolism showed higher abundance in the CP, in agreement with the NES cell model (Fig. 4*L*). FAS enzymes exhibited a slight upregulation in the CP (Fig. 4*M*), with only FASN being more abundant in the VZ, also in agreement with the NES cell model. The cholesterol synthesis pathway was a prerogative of VZ only, as expected (Fig. 4*N*). The PPP enzymes TKT, PGD, and PGLS were upregulated in the CP, with TALDO1 and G6PD showing minor modifications (Fig. 4*O*).

By examining specifically the proteins involved in neurogenesis, it was possible to estimate a temporal correlation between the expression profiles of neurons in the NES cell model and the CP neurons at 11 PCW. The longitudinal data of the neurogenesis-annotated proteins from the 2D model were analyzed by PCA and revealed the transition from NES cells to neurons along PC1 (Fig. 1*K*). The projection of the data from the CP neurons of the 11 PCW NCX onto this PCA score plot revealed that the CP neurons displayed a neurogenesis-protein signature similar to DIV30 to DIV60-neurons (*SI Appendix*, Fig. S14*A*). Similarly, a comparison of the fold changes of individual proteins in the 2D model and the fold change between the CP and VZ of the 11 PCW NCX revealed extensive consistency between the 2D model and fetal protein signatures for both neurogenesis proteins and the major metabolic enzymes (*SI Appendix*, Fig. S14*B*), thereby validating the metabolic arrangement profiled with NES cells.

Overall, quantitative proteomics of the human developing NCX highlighted a neuronal/metabolic profile that largely matched with our NES cells culture system and assigned a neuronal/metabolic identity of the CP neuronal population compatible with a sample in mid-neurogenesis (DIV60). In addition, the NAD(P)H FLIM approach proved applicable to cerebral tissue to obtain a spatial map of the diverse metabolic states.

Discussion

In our cell model, NAD(P)H FLIM and proteomics confirmed glycolysis as the preponderant energy source in NES cells and registered a shift toward OXPHOS during neuronal differentiation, in agreement with previous reports (10, 48). However, we observed that glycolysis was not entirely abrogated over time, but rather reconfigured according to a peculiar regulatory pattern. The abundance of enzymes in the first four steps of the preparatory phase (HK1, GPI PFKM, and the brain-specific isoform ALDOC) was largely preserved or increased during differentiation, while enzymes in the subsequent payoff phase were coordinately downregulated, except for the neuron-specific isoform ENO2 and PKM1, more abundant in neurons compared to PKM2. Triosephosphate isomerase 1 (TPI1), unlike other preparatory enzymes, diminished its abundance with differentiation, likely because its

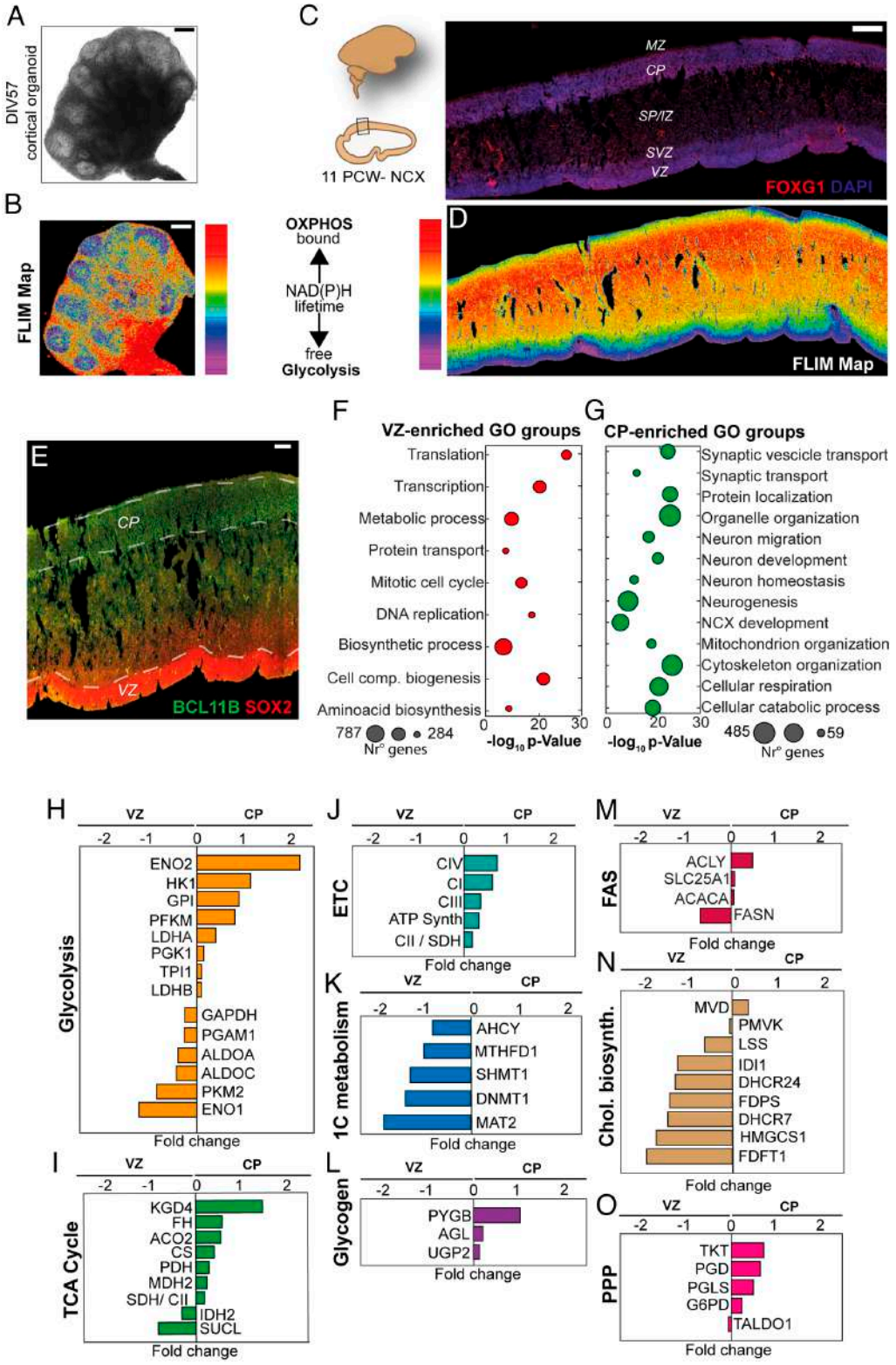

Fig. 4. NAD(P)H FLIM and proteomic analysis on human developing cortex and cerebro-cortical organoids. (*A*) Bright-field image of a 300 μm thick section of DIV57 acutely-sliced cerebro-cortical organoid, where neural rosettes are visible. (*B*) NAD(P)H FLIM metabolic map of the human cerebro-cortical organoid slice shown in (*A*). Rosettes rich in progenitors prioritize glycolytic metabolism, whereas external neuronal layers prefer OXPHOS. (*C*) Schematic representing a human early fetal brain and telencephalic coronal hemisection. Immunofluorescence staining of an 11 PCW brain coronal section with FOXG1 labeling the germinative telencephalic areas. (*D*) NAD(P)H FLIM metabolic map of the 11 PCW NCX showing a predominance of glycolytic metabolism in the ventricular zone (VZ) and a progressive transition to oxidative metabolism in the cortical plate (CP). (*E*) Immunofluorescence of the 11 PCW NCX, with BCL11B staining the CP and SOX2 the VZ. (*F*) Gene Ontology (GO) analysis of the VZ-enriched proteins. (*G*) GO analysis of the CP-enriched proteins. (*H*) Glycolysis protein fold changes in CP *vs.* VZ. (*I*) TCA cycle enzyme fold changes in CP vs. VZ. (*J*) Electron transport chain (ETC) protein fold changes in CP vs. VZ. (*K*) 1C metabolism enzyme fold changes in CP vs. VZ. (*L*) Glycogen metabolism protein fold changes in CP *vs.* VZ. (*M*) Fatty acid synthesis (FAS) enzyme fold changes in CP vs. VZ. (*N*) Cholesterol biosynthesis protein fold changes in CP vs. VZ. (*O*) Pentose-phosphate pathway (PPP) protein fold changes in CP *vs.* VZ. [Scale bars: 500 μm (*A*) and (*B*), 200 μm (*C*) and (*E*).]

substrate, dihydroxyacetone phosphate (DHAP), serves lipid synthesis, required for biomass production mostly in dividing cells.

While the bimodal behavior of the glycolysis contrasts with previous transcriptional analyses that reported its global reduction with neuronal differentiation (13), we speculate that this functional decoupling serves a biological purpose. In progenitors, the ATP-consuming preparatory phase represents a significant energetic cost. As maturing neurons switch to ETC, the cell could invest more energy in the preparatory phase. This allows metabolic intermediates of the preparatory phase to be redirected into the PPP, as supported by the growing abundance of HK1 and GPI over differentiation, and by the significant augmentation of glucose- and fructose-phosphate, two metabolites that glycolysis shares with PPP. Similarly, several other PPP intermediates, and S7P in particular, increased, thereby suggesting a shift toward alternative routes for glucose oxidation, which can restore glutathione antioxidant power through NADPH reduction. Collectively, these findings suggest the early activation of neuroprotective pathways, as also supported by the overexpression of several aldehyde dehydrogenases. These proteins play a crucial role in many biological processes including detoxification, ROS protection, and neurotransmitter biosynthesis (53–55), and it can be rationalized that they constitute a defense mechanism as neurons adapt to OXPHOS. Of note, the importance of PPP in contributing to metabolic rearrangements of corticogenesis was also reported in organoids (6), endorsing a role for this pathway in regulating neural stem cell maturation and its downstream choice of cell fate.

The payoff phase of glycolysis, characterized by ATP and NADH regeneration, was clearly associated with progenitors, as it constitutes their primary source of ATP. As neurons mature and switch to OXPHOS, the expression of this entire module is coordinately downregulated and the relative metabolites decrease. This metabolic transition is further facilitated by parallel adaptations in pyruvate metabolism. The conversion of pyruvate to lactate, mediated by LDHA, is pivotal in highly proliferative progenitors (12, 56), and its downregulation is a defined hallmark of neural differentiation (10). A similar trend was observed in our NES cell model, where LDHA temporal expression correlated positively with proliferative markers and negatively with neuronal proteins. Conversely, LDHB, which promotes the reverse reaction by converting lactate to pyruvate to fuel the TCA cycle (7, 57), increased over the course of differentiation. This finding was also corroborated by the quantification of lactate-to-pyruvate ratio at DIV30, confirming that major metabolic reshaping, including reduction of the Warburg effect, occurs early during differentiation and long before the acquisition of functional maturity. Accordingly, longer NAD(P)H lifetimes, indicative of OXPHOS, were already detectable at DIV30, alongside extensive changes to the cell's proteome.

When pyruvate is no longer converted to lactate, it enters the TCA cycle. Interestingly, while we observed that the abundance of the TCA cycle enzymes increased progressively, most of its metabolites were reduced by DIV30 compared to DIV0. We acknowledge that these metabolomics measurements were conducted on cells cultured in different media compositions according to the differentiation protocol, a factor that represents a potential limitation. However, several lines of evidence suggest that this trend reflects an intrinsic metabolic shift, rather than a media-driven artifact. First, glucose concentration remained constant, ensuring no bias for our interpretation of glycolysis and PPP. Second, although glutamine concentration doubled at DIV30, its metabolic role undergoes fundamental shift: while in proliferating progenitors (DIV0) glutamine could fuel the TCA cycle via glutaminolysis (58, 59), sustaining high levels of intermediates despite lower enzyme abundance, in neurons (DIV30) it is primarily diverted toward neurotransmitter replenishment (60, 61). The fact that TCA intermediates decrease precisely when extracellular glutamine increases reinforces the conclusion that this remodeling is dictated by intrinsic cellular programs. Furthermore, considering the global shift toward OXPHOS with its higher ATP yield per glucose unit, the reduction of TCA cycle intermediates likely reflects a more efficient oxidative metabolism rather than a decrease in energetic capacity.

While OXPHOS exhibited progressive upregulation over time, anabolic processes underwent rapid suppression, coincident with the onset of differentiation. Notably, lipid and nucleotide biosynthetic pathways—essential for proliferating progenitors—were markedly downregulated by DIV30. This pattern aligns with the inherent neurogenicity of NES cells, reinforcing the notion that metabolic remodeling is dictated by intrinsic cellular programs. Intriguingly, while cholesterol biosynthetic enzymes were rapidly downregulated by DIV30, cholesterol levels were paradoxically elevated in DIV30 cells compared to NES progenitors. We speculate that cholesterol may exert transcriptional feedback inhibition via SREBP-2 on its own biosynthetic pathway (62), while simultaneously accumulating in postmitotic cells where slower membrane turnover and reduced cholesterol catabolism allow its retention over extended periods (63).

Crucially, the physiological relevance of these metabolic trajectories is further validated by the consistency between our in vitro data and the 11 PCW fetal tissue, which is not subject to culture media variations. The 11 PCW human brain tissue section presented two major advantages: a clear spatial distinction between progenitors (VZ) and neurons (CP) and the presence in the CP of a relatively pure neuronal progeny since gliogenesis has not yet started (64). Although the comparison is based on a single human neocortical sample, the expression of metabolic enzymes in the CP and VZ highlighted numerous similarities with the trends observed in the cellular model. The upregulation of TCA cycle and ETC enzymes in the CP was confirmed, as was the bimodal behavior of glycolysis. Regarding the latter, we found a significant increase in HK consistent with NES cell data. Also, other enzymes of the initial steps of glycolysis (PFKM and GPI) were increased in the CP compared to the VZ, similar to the cellular model. Among these, unexpectedly, LDHA exhibited a slight augmented expression in the CP compared to the VZ, whereas in the cellular model LDHA expression quickly decreased upon NES cell differentiation. We speculate that this difference could be ascribed to a still incomplete vascularization of the tissue and suboptimal oxygenation favoring anaerobic glycolysis. Of note, PPP enzymes were expressed at higher levels in the CP than in the VZ, as were glycogen breakdown enzymes, thus corroborating the hypothesis of a role in neural protection and energetic support in keeping with our proteomics and metabolomics data collected from NES cells. Anabolic pathways including 1C metabolism, cholesterol biosynthesis and the activity of fatty acid synthase were expectedly upregulated in the VZ.

The application of NAD(P)H FLIM on human NCX allowed the construction of a visual map of the metabolic rearrangements that occur during corticogenesis integrated with conventional immunofluorescence imaging. The spatial separation between a glycolytic VZ and an OXPHOS zone — spanning from the IZ to the CP — provided direct imaging evidence of how metabolism transitions along neocortical radial differentiation.

While our study provided a proof of principle of the applicability of NAD(P)H FLIM to human brain, we acknowledge that further investigations are needed on diverse *postmortem* samples at different stages of corticogenesis for a wider perspective of how metabolism accommodates neuronal development, migration, and layer formation. Additionally, although our study primarily focused

on neural progenitors and neuronal differentiation, the contribution of astrocytes to CNS metabolism warrants recognition. We believe that future complementary investigations should specifically address the dynamic regulation of metabolic pathways in glial cells, thus providing a wider perspective of their contribution to metabolism rewiring.

Considering the global effort toward the understanding of neurodevelopmental metabolic diseases and personalized medicine, we provided evidence that NAD(P)H FLIM could be applied to differentiating hiPSCs as well as cerebro-cortical organoids, thus opening the path to its application on patient-derived cells. In this regard, NAD(P)H FLIM could prove useful in the case of comparative physiopathology studies, allowing metabolic differences and responses to treatment to be monitored in real-time and in an almost noninvasive manner.

In conclusion, we have illustrated how the metabolic pathways of the human NCX adapt during development in physiological conditions through a model that closely retraces corticogenesis in vivo. We envision that this study may provide a valuable resource for future investigations of neurodevelopmental conditions linked to metabolic failure or energetic imbalance and pave the path for innovative therapeutic approaches.

Ethics Statement. All cell work was performed according to NIH guidelines for the acquisition and distribution of human tissue for biomedical research purposes and with approval by the Human Investigation Committee and Institutional Ethics Committee of each institution from which the samples were obtained (University of Pisa Review No. 18/2020). Appropriate informed consent was obtained, and all available nonidentifying information was recorded for each specimen. The tissue was handled in accordance with the ethical guidelines and regulations for the research use of human brain tissue set forth by the NIH and the WMA Declaration of Helsinki.

The human tissue brain sections used in this study derive from postmortem specimens obtained by the Human Developmental Biology Resource (www.hdbr.org).

Materials and Methods

A detailed description of Material and Methods is included in *SI Appendix*. Briefly, NES cells were cultured and differentiated as previously described (26, 28). iPSC were expanded and differentiated as reported (24, 34). The FLIM analysis was conducted using the Picoquant excitation laser, powered by a PDL 828 Sepia II laser driver. The proteomics analysis was conducted using an Orbitrap Fusion (Thermo Scientific) coupled to an Easy-nLC 1000 (Thermo Scientific). The metabolomics analysis was performed by gas chromatography coupled with mass spectrometry single quadrupole (GC 7890/MS 5975C, Agilent).

Data, Materials, and Software Availability. Proteomic data have been deposited in PRIDE (PXD058952) (65). Other data are included in the article and/or supporting information.

ACKNOWLEDGMENTS. We thank Dr. Angelo Valetto for performing the NES cell karyotype analysis. We thank Prof. Massimo Pasqualetti and Dr. Sara Migliarini for helping with sample processing. We thank Samantha Pezzica for help with metabolomics experiments. We thank "Margherita silenziosa" Association for supporting Fondazione Pisana per la Scienza laboratories. This work was supported by Fondazione Pisana per la Scienza (FPS) Seed Grant (to M.T.D.). FPS received support from the European Union- Next Generation EU, mission 4 component 2 Inv. 1.5 CUP: B13D21011850006. M.O. laboratory received support from the European Union Next-Generation EU, National Recovery and Resilience Plan (NRRP), mission 4, component 2, investment 1.4 ("Tuscany Health Ecosystem," CUP N. B83C22003930001), and investment 1.1, call PRIN 2022 PNRR (D.D. 1409 14-09-2022–Uncovering spatial and temporal sequence of neurodegeneration in a 3D model of corticospinal-neuromuscular unit of Amyotrophic Lateral Sclerosis–Prot. P2022MSFT3 CUP I53D23006630001). F.C. laboratory received support from the European Research Council (ERC) under the European Union's Horizon 2020 research and innovation program (grant agreement No 866127, project CAPTUR3D). The human embryonic and fetal material was provided by the Joint MRC/Wellcome Trust (grant# MR/R006237/1) Human Developmental Biology Resource (www.hdbr.org). This manuscript reflects only the authors' views and opinions; neither the European Union nor the European Commission can be considered responsible for them.

Author affiliations: [a]Fondazione Pisana per la Scienza ONLUS, San Giuliano Terme, Italy 56017, Italy; [b]Fondazione Toscana Gabriele Monasterio, Pisa 56124, Italy; [c]Department of Biology Unit of Cell, Molecular and Developmental Biology, University of Pisa, Pisa 56127, Italy; [d]Institute of Clinical Physiology, National Research Council, Pisa 56124, Italy; [e]Department of Translational Research and New Technologies in Medicine and Surgery, University of Pisa, Pisa 56123, Italy; [f]Department of Pharmacy, University of Pisa, Pisa 56126, Italy; and [g]National Enterprise for nanoScience and nanoTechnology Laboratory, Scuola Normale Superiore, Pisa 56127, Italy

Author contributions: M.T.D. designed research; G.F., F.F., F.G., A.Z., F. Carli, E.D., F.O., and G.C.D. performed research; A.G. contributed new reagents/analytic tools; G.F., F.F., F.G., A.Z., F. Carli, A.P., E.D., F.O., R.D., A.S., G.C.D., A.G., F. Cardarelli, M.O., L.A.M., and M.T.D. analyzed data; and G.F., and M.T.D. wrote the paper.

1. L. Traxler *et al.*, Metabolism navigates neural cell fate in development, aging and neurodegeneration. *Dis. Model. Mech.* **14**, dmm048993 (2021).
2. S. Herculano-Houzel, Scaling of brain metabolism with a fixed energy budget per neuron: Implications for neuronal activity, plasticity and evolution. *PLoS One* **6**, e17514 (2011).
3. T. Namba, J. Nardelli, P. Gressens, W. B. Huttner, Metabolic regulation of neocortical expansion in development and evolution. *Neuron* **109**, 408–419 (2021).
4. C. A. Perez-Ramirez *et al.*, Atlas of fetal metabolism during mid-to-late gestation and diabetic pregnancy. *Cell* **187**, 204–215.e14 (2024).
5. M. Khacho *et al.*, Mitochondrial dynamics impacts stem cell identity and fate decisions by regulating a nuclear transcriptional program. *Cell Stem Cell* **19**, 232–247 (2016).
6. J. Mil *et al.*, Metabolic atlas of early human cortex identifies regulators of cell fate transitions. bioRxiv [Preprint] (2025). https://doi.org/10.1101/2025.03.10.642470 (Accessed 20 January 2026).
7. R. Iwata *et al.*, Mitochondria metabolism sets the species-specific tempo of neuronal development. *Science* **379**, eabn4705 (2023).
8. M. Götz, W. B. Huttner, The cell biology of neurogenesis. *Nat. Rev. Mol. Cell Biol.* **6**, 777–788 (2005).
9. J. C. Silbereis, S. Pochareddy, Y. Zhu, M. Li, N. Sestan, The cellular and molecular landscapes of the developing human central nervous system. *Neuron* **89**, 248–268 (2016).
10. Z. Molnár *et al.*, New insights into the development of the human cerebral cortex. *J. Anat.* **235**, 432–451 (2019).
11. P. Gao, K. T. Sultan, X.-J. Zhang, S.-H. Shi, Lineage-dependent circuit assembly in the neocortex. *Development* **140**, 2645–2655 (2013).
12. C. Maffezzini, J. Calvo-Garrido, A. Wredenberg, C. Freyer, Metabolic regulation of neurodifferentiation in the adult brain. *Cell. Mol. Life Sci.* **77**, 2483–2496 (2020).
13. X. Zheng *et al.*, Metabolic reprogramming during neuronal differentiation from aerobic glycolysis to neuronal oxidative phosphorylation. *Elife* **5**, e13374 (2016).
14. C. Garone, F. De Giorgio, S. Carli, Mitochondrial metabolism in neural stem cells and implications for neurodevelopmental and neurodegenerative diseases. *J. Transl. Med.* **22**, 238 (2024).
15. M. Bélanger, I. Allaman, P. J. Magistretti, Brain energy metabolism: Focus on astrocyte-neuron metabolic cooperation. *Cell Metab.* **14**, 724–738 (2011).
16. P. Mergenthaler, U. Lindauer, G. A. Dienel, A. Meisel, Sugar for the brain: The role of glucose in physiological and pathological brain function. *Trends Neurosci.* **36**, 587–597 (2013).
17. K. M. Candelario, C. W. Shuttleworth, L. A. Cunningham, Neural stem/progenitor cells display a low requirement for oxidative metabolism independent of hypoxia inducible factor-1alpha expression. *J. Neurochem.* **125**, 420–429 (2013).
18. W. Zhou *et al.*, TIGAR promotes neural stem cell differentiation through acetyl-CoA-mediated histone acetylation. *Cell Death Dis.* **10**, 198 (2019).
19. L. Traxler *et al.*, Warburg-like metabolic transformation underlies neuronal degeneration in sporadic Alzheimer's disease. *Cell Metab.* **34**, 1248–1263.e6 (2022).
20. W. J. H. Koopman, F. Distelmaier, J. A. M. Smeitink, P. H. G. M. Willems, OXPHOS mutations and neurodegeneration. *EMBO J.* **32**, 9–29 (2013).
21. P. J. Magistretti, I. Allaman, A cellular perspective on brain energy metabolism and functional imaging. *Neuron* **86**, 883–901 (2015).
22. T. S. Cliff, S. Dalton, Metabolic switching and cell fate decisions: Implications for pluripotency, reprogramming and development. *Curr. Opin. Genet. Dev.* **46**, 44–49 (2017).
23. I. Angelopoulos *et al.*, Metabolic regulation of the neural stem cell fate: Unraveling new connections, establishing new concepts. *Front. Neurosci.* **16**, 1009125 (2022).
24. S. M. Chambers *et al.*, Highly efficient neural conversion of human ES and iPS cells by dual inhibition of SMAD signaling. *Nat. Biotechnol.* **27**, 275–280 (2009).
25. J. G. Camp *et al.*, Human cerebral organoids recapitulate gene expression programs of fetal neocortex development. *Proc. Natl. Acad. Sci. U.S.A.* **112**, 15672–15677 (2015).
26. M. Onorati *et al.*, Zika virus disrupts Phospho-TBK1 localization and mitosis in human neuroepithelial stem cells and radial glia. *Cell Rep.* **16**, 2576–2592 (2016).
27. C. Stringari *et al.*, Phasor approach to fluorescence lifetime microscopy distinguishes different metabolic states of germ cells in a live tissue. *Proc. Natl. Acad. Sci. U.S.A.* **108**, 13582–13587 (2011).

28. M. T. Dell'Anno *et al.*, Human neuroepithelial stem cell regional specificity enables spinal cord repair through a relay circuit. *Nat. Commun.* **9**, 3419 (2018).
29. M. Onorati *et al.*, Molecular and functional definition of the developing human striatum. *Nat. Neurosci.* **17**, 1804–1815 (2014).
30. J. Tailor *et al.*, Stem cells expanded from the human embryonic hindbrain stably retain regional specification and high neurogenic potency. *J. Neurosci.* **33**, 12407–12422 (2013).
31. S. Ranjit, L. Malacrida, D. M. Jameson, E. Gratton, Fit-free analysis of fluorescence lifetime imaging data using the phasor approach. *Nat. Protoc.* **13**, 1979–2004 (2018).
32. G. Ferri *et al.*, Metabolic response of Insulinoma 1E cells to glucose stimulation studied by fluorescence lifetime imaging. *FASEB Bioadv.* **2**, 409–418 (2020).
33. C. Stringari, P. Donovan, E. Gratton, "Phasor FLIM metabolic mapping of stem cells and cancer cells in live tissues" in *Proceedings Volume 8226, Multiphoton Microscopy in the Biomedical Sciences XII*, A. Periasamy, K. König, P. T. C. So, Eds. (SPIE, 2012), p. 82260D.
34. A. M. M. Sousa *et al.*, Molecular and cellular reorganization of neural circuits in the human lineage. *Science* **358**, 1027–1032 (2017).
35. C. Dell'Amico *et al.*, Microcephaly-associated protein WDR62 shuttles from the Golgi apparatus to the spindle poles in human neural progenitors. *Elife* **12**, e81716 (2023).
36. A. A. Wani, Comprehensive analysis of clustering algorithms: Exploring limitations and innovative solutions. *PeerJ Comput. Sci.* **10**, e2286 (2024).
37. M. D. Shahbazian, B. Antalffy, D. L. Armstrong, H. Y. Zoghbi, Insight into Rett syndrome: MeCP2 levels display tissue- and cell-specific differences and correlate with neuronal maturation. *Hum. Mol. Genet.* **11**, 115–124 (2002).
38. V. Vukojevic *et al.*, Evolutionary conserved role of neural cell adhesion molecule-1 in memory. *Transl. Psychiatry* **10**, 217 (2020).
39. S. M. Ferguson, Neuronal lysosomes. *Neurosci. Lett.* **697**, 1–9 (2019).
40. G. A. Wayman, Y.-S. Lee, H. Tokumitsu, A. J. Silva, T. R. Soderling, Calmodulin-kinases: Modulators of neuronal development and plasticity. *Neuron* **59**, 914–931 (2008).
41. C. M. Drerup, A. L. Herbert, K. R. Monk, A. V. Nechiporuk, Regulation of mitochondria-dynactin interaction and mitochondrial retrograde transport in axons. *Elife* **6**, e22234 (2017).
42. H. G. Lebherz, W. J. Rutter, Distribution of fructose diphosphate aldolase variants in biological systems. *Biochemistry* **8**, 109–121 (1969).
43. D. Oliva, L. Calì, S. Feo, A. Giallongo, Complete structure of the human gene encoding neuron-specific enolase. *Genomics* **10**, 157–165 (1991).
44. T. C. Genaro-Mattos, A. Anderson, L. B. Allen, Z. Korade, K. Mirnics, Cholesterol biosynthesis and uptake in developing neurons. *ACS Chem. Neurosci.* **10**, 3671–3681 (2019).
45. F. W. Pfrieger, Outsourcing in the brain: Do neurons depend on cholesterol delivery by astrocytes? *Bioessays* **25**, 72–78 (2003).
46. Z. Chen *et al.*, Brain energy metabolism: Astrocytes in neurodegenerative diseases. *CNS Neurosci. Ther.* **29**, 24–36 (2023).
47. E. Lionaki, C. Ploumi, N. Tavernarakis, One-carbon metabolism: Pulling the strings behind aging and neurodegeneration. *Cells* **11**, 214 (2022).
48. A. S. Almeida *et al.*, Improvement of neuronal differentiation by carbon monoxide: Role of pentose phosphate pathway. *Redox Biol.* **17**, 338–347 (2018).
49. V. Xanthis, T. Mantso, A. Dimtsi, A. Pappa, V. E. Fadouloglou, Human aldehyde dehydrogenases: A superfamily of similar yet different proteins highly related to cancer. *Cancers (Basel)* **15**, 4419 (2023).
50. C.-C. Chiu *et al.*, Neuroprotective effects of aldehyde dehydrogenase 2 activation in rotenone-induced cellular and animal models of parkinsonism. *Exp. Neurol.* **263**, 244–253 (2015).
51. I. Bystron, C. Blakemore, P. Rakic, Development of the human cerebral cortex: Boulder Committee revisited. *Nat. Rev. Neurosci.* **9**, 110–122 (2008).
52. J. Calvo-Garrido *et al.*, SQSTM1/p62-directed metabolic reprogramming is essential for normal neurodifferentiation. *Stem Cell Rep.* **12**, 696–711 (2019).
53. R. Deza-Ponzio, M. L. Herrera, M. J. Bellini, M. B. Virgolini, C. B. Hereñú, Aldehyde dehydrogenase 2 in the spotlight: The link between mitochondria and neurodegeneration. *Neurotoxicology* **68**, 19–24 (2018).
54. F. A. Dingler *et al.*, Two aldehyde clearance systems are essential to prevent lethal formaldehyde accumulation in mice and humans. *Mol. Cell* **80**, 996–1012.e9 (2020).
55. J. Nakamura, D. W. Holley, T. Kawamoto, S. J. Bultman, The failure of two major formaldehyde catabolism enzymes (ADH5 and ALDH2) leads to partial synthetic lethality in C57BL/6 mice. *Genes Environ.* **42**, 21 (2020).
56. M. G. Vander Heiden, L. C. Cantley, C. B. Thompson, Understanding the Warburg effect: The metabolic requirements of cell proliferation. *Science* **324**, 1029–1033 (2009).
57. C. J. Valvona, H. L. Fillmore, P. B. Nunn, G. J. Pilkington, The regulation and function of Lactate Dehydrogenase A: Therapeutic potential in brain tumor. *Brain Pathol.* **26**, 3–17 (2016).
58. T. Namba *et al.*, Human-specific ARHGAP11B acts in mitochondria to expand neocortical progenitors by glutaminolysis. *Neuron* **105**, 867–881.e9 (2020).
59. N. Journiac *et al.*, Cell metabolic alterations due to Mcph1 mutation in microcephaly. *Cell. Rep.* **31**, 107506 (2020).
60. H. S. Waagepetersen, H. Qu, U. Sonnewald, K. Shimamoto, A. Schousboe, Role of glutamine and neuronal glutamate uptake in glutamate homeostasis and synthesis during vesicular release in cultured glutamatergic neurons. *Neurochem. Int.* **47**, 92–102 (2005).
61. D. L. Rothman, H. M. De Feyter, R. A. de Graaf, G. F. Mason, K. L. Behar, 13C MRS studies of neuroenergetics and neurotransmitter cycling in humans. *NMR Biomed.* **24**, 943–957 (2011).
62. M. S. Brown, J. L. Goldstein, The SREBP pathway: Regulation of cholesterol metabolism by proteolysis of a membrane-bound transcription factor. *Cell* **89**, 331–340 (1997).
63. L. Qian, A. B. Chai, I. C. Gelissen, A. J. Brown, Balancing cholesterol in the brain: From synthesis to disposal. *Explor. Neuroprot. Ther.* **22**, 1–27 (2022), 10.37349/ent.2022.00015.
64. C. B. Holst, C. B. Brøchner, K. Vitting-Seerup, K. Møllgård, Astrogliogenesis in human fetal brain: Complex spatiotemporal immunoreactivity patterns of GFAP, S100, AQP4 and YKL-40. *J. Anat.* **235**, 590–615 (2019).
65. F. Greco, L. McDonnell, Metabolic trajectories in human neocortical development. PRIDE (Proteomics Identifications Database). https://www.ebi.ac.uk/pride/archive/projects/PXD058952. Deposited 17 December 2024.